MNRAS **000**, 1–10 (2019) Preprint 12 April 2019 Compiled using MNRAS LATEX style file v3.0

ON THE GEOMETRY OF THE X-RAY EMISSION FROM PULSARS
The Changing Aspect of the Be/X-ray Pulsar SXP348

R. Cappallo,[1,2]⋆ S. G. T. Laycock,[1,2] D. M. Christodoulou[2,3] M. J. Coe[4] and A. Zezas[5,6]
[1]*Department of Physics and Applied Physics, University of Massachusetts Lowell, Lowell MA, 01854, USA*
[2]*Lowell Center for Space Science and Technology, 600 Suffolk Street, Lowell MA, 01854, USA*
[3]*Department of Mathematical Sciences, University of Massachusetts Lowell, Lowell MA, 01854, USA*
[4]*School of Physics and Astronomy, Southampton University, Highfield, Southampton, SO17 1BJ, UK*
[5]*Physics Department & Institute of Theoretical & Computational Physics, University of Crete, 71003 Heraklion, Crete, Greece*
[6]*Harvard-Smithsonian Center for Astrophysics, 60 Garden Street, Cambridge MA, 02138, USA*

Accepted XXX. Received YYY; in original form ZZZ

ABSTRACT
The X-ray source SXP348 is a high-mass X-ray binary system in the Small Magellanic Cloud. Since its 1998 discovery by *BeppoSAX*, this pulsar has exhibited a spin period of $\sim 340 - 350$ s. In an effort to determine the orientation and magnetic geometry of this source, we used our geometric model *Polestar* to fit 71 separate pulse profiles extracted from archival *Chandra* and *XMM-Newton* observations over the past two decades. During 2002 pulsations ceased being detectable for nine months despite the source remaining in a bright state. When pulsations resumed, our model fits changed, displaying a change in accretion geometry. Furthermore, in 2006 detectable pulsations again ceased, with 2011 marking the last positive detection of SXP348 as a point source. These profile fits will be released for public use as part of the database of Magellanic Cloud pulsars.

Key words: accretion, accretion disks – methods: numerical – stars: magnetic field – stars: neutron – pulsars: general – X-rays: binaries

1 INTRODUCTION

High-mass X-ray binaries (HMXBs) are double stars comprised of a neutron star (NS) or black hole (BH) and a massive companion star orbiting around their mutual center of mass (see, e.g., Reig (2011), and references therein). In these systems, the compact object accretes matter from the companion, converting a significant fraction of gravitational potential energy into radiation, predominately as X-rays. Since 1970 a succession of Earth-orbiting telescopes have observed these X-rays revealing time-dependent variations in flux.

In the case of a neutron star, accreted matter is funneled along magnetic field lines onto the magnetic poles at the NS surface. At high enough luminosities ($L_X \gtrsim 10^{36}$ erg s^{-1}) a shock is created above the NS surface and an accretion column forms below this shock (Basko & Sunyaev 1976). This "critical luminosity" (Reig & Milonaki 2016) marks the formation point for the column, with accompanying "fan-beam" emission radiating from its sides. Below this critical luminosity ($L_{\rm crit}$) the majority of the emission is normal to the NS surface (i.e. "pencil-beam" emission). The precise critical luminosity is different for each system and its range is a key factor for understanding the state transitions and energetics of these systems. In fact, there are two luminosities in an HMXB system that may be considered "critical".

Reig & Nespoli (2013) identify two distinct tracks for HMXBs in the hardness intensity diagram: the horizontal (low luminosity) branch (HB), characterized by rapid variability and hardness correlated to luminosity, and the diagonal branch (DB) which extends up to the highest luminosities, the source getting softer with increasing luminosity. The transition from the HB to the DB empirically defines a critical luminosity (for an individual source). Although their landmark study used data obtained during giant (Type II) outbursts, there is no *a priori* reason to suppose that the states would not apply to normal outbursts.

Becker et al. (2012) derived a critical luminosity marking the formation of a radiatively dominated shock, connected with the formation of an accretion column, several km in height. The actual value of $L_{\rm crit}$ is some fraction of

⋆ E-mail: rigelcappallo@gmail.com

the Eddington luminosity, depending upon the magnetic field strength, through both its effect on (a) the scattering cross section, and (b) its constriction of the accretion flow. In support of this concept applying to the empirical state transition, all observations of the DB have occurred for $L_X/L_{crit} >> 1$ (Reig & Nespoli 2013). Observations show that the DB can occur for $L_X > 50$ PCU counts s^{-1} (approx. 10^{37} erg s^{-1}) for KS1947+300, the lowest in their sample, while some sources (e.g. A0535+26) remain in the HB despite exceeding several 10^{37} erg s^{-1}. This fact indicates an order of magnitude spread in the B-fields of accreting pulsars. Cyclotron line studies also support this interpretation (e.g. Rothschild et al. (2017); Vybornov et al. (2017)). The behavior of pulsars on the HB indicates that substantial spectral hardening can occur without the formation of an extended column. Thus whether the pulse profile undergoes a corresponding systematic change *below* the transition to the DB is an interesting, and for the moment, open question.

The focus of this paper is the X-ray bright source SXP348, a Be/X-ray binary (BeXRB) pulsar in the Small Magellanic Cloud (SMC). BeXRBs are the most prevalent subclass of HMXBs, comprising 70% and 90% of galactic and SMC HMXBs respectively. In these systems the donor stars are massive Be stars. These Be stars display emission lines in their optical spectrum owing to large circumstellar disks. In the case of BeXRBs, this disk supplies the material to the pulsar and may be truncated through tidal interaction (Reig 2011).

We have extracted light curves from archival *Chandra* and *XMM-Newton* observations and have used our geometric model *Polestar* described in Cappallo et al. (2017) (hereafter referred to as Paper I) in order to produce individual fits to 71 unique pulse profiles (see Table D1 for the ObsIDs and observation dates corresponding to these profiles). We have performed a statistical analysis of the results in an attempt to find the best-fit geometric parameters of the pulsar and the orientation of its magnetic field relative to its spin axis. In addition, we have explored the possibility of the emergence of steep features in the model fit as a marker of fan-beam emission at higher luminosity states, thus introducing a novel approach to determining a critical luminosity for SXP348.

In the following sections, we describe the analysis of the data set and the statistics of the results. §§ 1.1 and 1.2 are recaps of the literature on this system. In §§ 2-3, we describe the collection and treatment of the data used in this study, our geometric model, its free parameters, and the fitting procedure. In § 4 and § 5 we provide a detailed analysis of the fits and the long-term behavior of this source, followed by a discussion and our conclusions in § 6 and § 7, respectively. Some additional details on our model parameter space, period uncertainty, and parameter uncertainty along with parameter tables can be found in the Appendix.

1.1 SXP348

The X-ray source SXP348, also identified as SAX J0103.2-7209 = 2E 0101.5-7225 = RX J0103.2-7209 (Israel et al. 2000; Coe et al. 2005; McGowan et al. 2007), was discovered by *BeppoSAX* with a pulse period of (345.2 ± 0.1) s (Israel et al. 1998). Since that time, it is slowly spinning up on average at a rate of -0.1 s yr^{-1}(Yang et al. 2017), although various spin periods have been measured at different times: (348.9 ± 0.3) s (Yokogawa & Koyama 1998), (343.5 ± 0.5) s (Israel et al. 2000), (341.21 ± 0.50) s (Haberl & Pietsch 2004), and more recently (337.51 ± 5.17) s (McGowan et al. 2007), albeit at a lower than 90% significance.

Using *Chandra* ACIS-I data filtered at 0.3 - 8.0 keV, McGowan et al. (2007) produced a fit to the X-ray spectrum with an absorbed power law with photon index $\Gamma = 0.8$ resulting in an unabsorbed luminosity of $L_X \simeq 2.5 \times 10^{35}$ erg s^{-1}. A maximum luminosity of $L_X \simeq 1.0 \times 10^{36}$ erg s^{-1} was reported by Rajoelimanana et al. (2011). In the following analysis, we calculate $L_{X,max} \simeq 1.1 \times 10^{36}$ erg s^{-1}, assuming a distance to the SMC of 62 ± 3 kpc (Haschke, Grebel, & Duffau 2012). Owing to the small variations in luminosity over time, this system appears to exhibit a steady accretion rate when observed, suggesting a low eccentricity coupled with a wide orbit.

1.2 Optical Counterpart

SXP348 is coincident with the emission-line star [MA93] 1367, which has been identified as its binary companion. It is optically classified as a Be star with $V_{mag} = 14.8$ (Hughes & Smith 1994; Israel et al. 1998), spectral type B0.5, luminosity class IV - V (Rajoelimanana et al. 2011). It appears in the MACHO catalog as object 206.16776.17. This optical counterpart has shown variations in the Hα line during various observations, but the Hβ line has consistently shown an emission peak in all observations (Evans et al. 2004). From optical/IR OGLE II data, the orbital period of the system has been calculated as ∼ 94 d (Schmidtke & Cowley 2006) with an additional long-term variation of the optical light-curve on the order of ∼ 2000 d (Rajoelimanana et al. 2011).

2 DATA

We extracted the light curves from all available *Chandra* and *XMM-Newton* archival data of the BeXRB SXP348. The observation dates span MJD 51560 to 58228 (January 2000 to April 2018). The light curves were folded on periods found from a Lomb-Scargle periodogram analysis with detections at significance $s \geq$ %99. The details of the *Chandra* and *XMM-Newton* data extraction are given in §§ 2.1 and 2.2 of our SMC library paper (Yang et al. 2017), with the periodicity search described in § 2.4.1.

The results of the SXP348 pipeline will be made public as separate data products that include pulse profiles, model fits with residuals, and folded event files.

3 FITTING STRATEGY

Polestar is a physically motivated yet purely geometrical model with parameters controlling the hot-spot locations and the geometry of each emission region with fan and pencil-like components. Each of these parameters may be varied or kept fixed during the fitting procedure. In this work, the data were fitted with an antipodal hot-spot arrangement (two hot spots oriented along a single dipole axis passing through the center of the NS). A preliminary iteration was carried out with only four free parameters: the

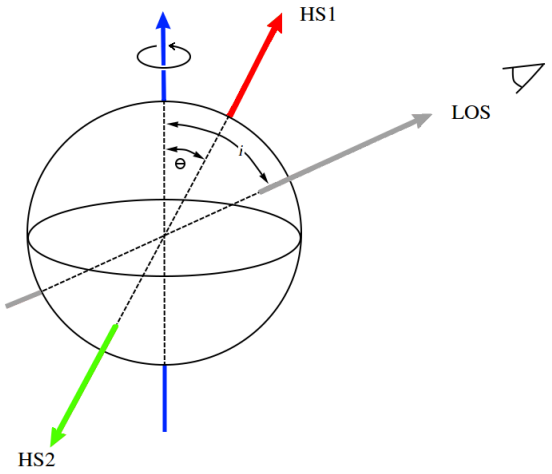

Figure 1. A diagram of the underlying geometry of *Polestar*. The blue vector is the spin axis, the grey vector is the line of sight (LOS) direction, and the red and green hot spot (HS) vectors match the red and green components displayed in the pulse profile fits. This particular orientation is representitive of the 6 parameter *Polestar* fit for *XMM-Newton* ObsID 0135721701 (Fig. 3).

inclination angle i of the spin axis to the line of sight, the inclination angle θ of the primary hot spot to the spin axis, the longitude ϕ of the primary hot spot from (the arbitrary) phase zero, and the power of the cosine beaming function P_{cos} (Paper I). For a visualization of this geometry see Fig. 1. The use of only a cosine function represents pencil-beam emission from the hot spots appropriate for lower luminosity ($L_X \leq 10^{36}$ erg s^{-1}) states (Zavlin et al. 1995). We note that *Polestar* does take light-bending effects into account using the approximation introduced in Beloborodov (2002).

A second iteration incorporated two additional parameters, the power of a sine beaming function representing fan-beam emission (P_{sin}), and the ratio of the two functions in the overall emission power (P_{rat}). This fan-beam emission represents radiation emitted from the sides of the accretion column and is appropriate for higher luminosity ($L_X \gtrsim 10^{36}$ erg s^{-1}) states (Ferrigno et al. 2011, and references therein). In these high-luminosity states some of the photons emitted parallel to the NS surface are trapped by the strong magnetic and gravitational fields and forced back down to the mound at the base of the accretion column. To some extent these photons are naturally incorporated into this model as they will re-radiate from this thermal mound as an additional component of the pencil-beam emission, however some photons may land further from the accretion mound and re-radiate as unpulsed emission from the NS surface (for a deeper discussion of this effect see Mushtukov et al. (2018)).

3.1 Fitting Algorithm

Each folded light curve was fit with *Polestar* using a modified coordinate descent algorithm (Bianchi et al. 2014). In the standard coordinate descent method (also known as a coordinatewise minimization) an initial guess is made in the parameter space, and then all but one of the parameters are held constant as the minimum is found for the varying parameter. This is performed for each parameter until all minima are located (Tseng 2001). For the fitting presented in this paper, an initial coarse fit was performed using brute-step minimization on the entire parameter space with a large mesh (known as a block coordinate descent) identifying the two lowest minima. Then a secondary fit was performed around these two minima with a much finer grid to pinpoint each local minimum. Finally, the lowest of these two minima was adopted as the global minimum. This is a reasonable approach provided that the fitting function does not suffer from large discontinuities (leading to deep spikes of local minima nestled in generally poor-fitting areas of the parameter space). In the case of only pencil-beam emission, this is a reasonable assumption. Once the fan beam is introduced, some discontinuities may arise associated with emission from poles that become visible only for a brief period of time.

In order to further verify that these minima were global, two alternative fitting techniques were applied multiple times, least squares and differential evolution (see Attia 2011, for a description of the latter technique) and the results were compared to the brute-step results. The alternative techniques never found a minimum lower than the one found by the brute-step method, and indeed sometimes found local minima that were not global.

4 MODEL ANALYSIS

In the adopted antipodal geometry, there is a degeneracy between inclination i and latitude of the primary hot spot θ (for more details see Appendix A). Despite the existence of this degeneracy, a single variable (e.g., the angle between the two axes) cannot describe the emission geometry exactly since, for example, a profile with $i = \theta = 30°$ is markedly different from another profile with $i = \theta = 60°$ (even though $i - \theta = 0$ in both cases). We proceeded with modeling of the folded light-curves as follows.

4.1 Four-Parameter Fit

The preliminary four-parameter fit was performed to characterize the gross geometry of the emission and identify possible patterns (Table D1). The four parameters that were allowed to vary were i and θ (both from 0° to 90°), the power of the cosine beaming function ($1 \leq P_{cos} \leq 3$), and the initial phase ($0° \leq \phi < 360°$).

Histograms of the inclination angle (i) and primary hot spot latitude (θ) for the 71 profiles both show prominent peaks around 35° with secondary and tertiary peaks at > 50° (Fig. 2). There is a reason for this dip around 50°. With an antipodal model using only a cosine beaming function (pencil beam), the width of the profile's peak and the depth of the trough in the resulting profile are governed by i and θ. If either of these angles is above 45°, then a second peak begins to emerge in the trough, eventually reaching the height of the primary peak when the magnetic dipole becomes orthogonal to the spin axis ($i = \theta = 90°$). Since no peak is observed in the profile's trough (see, e.g., Figs. 3 & 4), angles around 50° for i and θ are not preferred.

The peaks in these profiles generally display a sharper

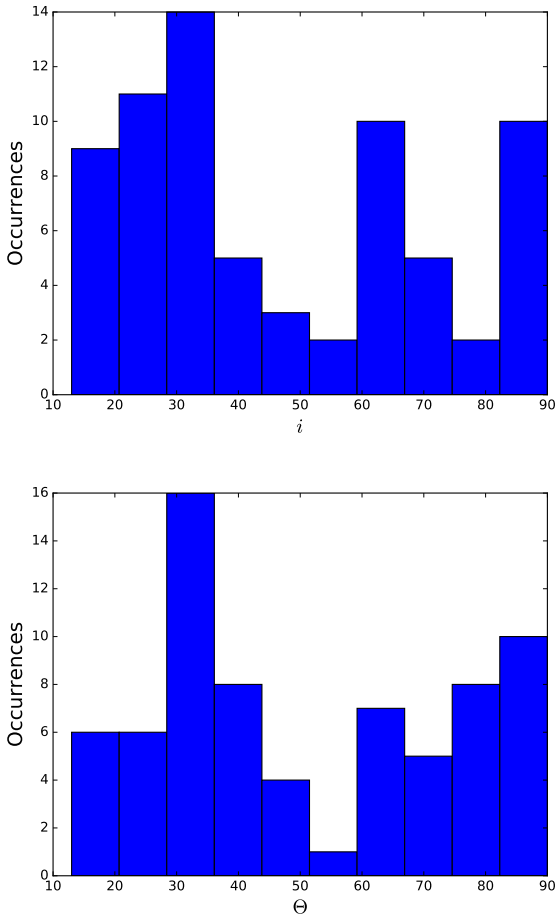

Figure 2. Histograms of values for the inclination angle (i, top) and the angle between the spin axis and the magnetic dipole axis (θ, bottom) for the 4-parameter *Polestar* fits for all 71 observations.

drop (i.e., steeper sides) than can be accommodated by a pure cosine beaming function. On the other hand, such eclipse-like drops are often seen when a fan beam is activated and a pole crosses the terminator (see Paper I for details on this effect). This fact was the impetus for refitting the data with two additional parameters that incorporated the fan-beam sine function.

4.2 Six-Parameter Fit

The 6-parameter fit incorporated the power of the sine beaming function (P_{sin}) and the ratio of the contributions by both the cosine and sine functions to the overall profile (P_{rat}). With this extension, the model's behavior becomes more complex leading to significantly better fits (Table D2). The various parameters have the following manifestations in the resulting profile:

For an antipodal geometry that allows both sine and cosine beaming functions, the width of the peak is primarily governed by $\max(i, \theta)$. At a maximum of $\approx 35°$, this width is one-half of the phase. As i or θ increases (i.e., as the line of sight or the hot spot moves towards the equator), the peak

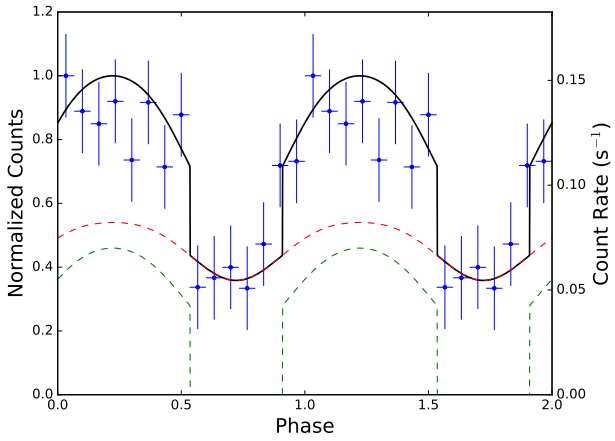

Figure 3. A 6-parameter *Polestar* model fit with $i = 50°$ and $\theta = 20°$. The data, with error on count rate and bin-size, are in blue. The model fit is in black, with the contributions of the two hot spots in red and green dashed lines. This profile is for *XMM-Newton* ObsID 0135721701 (see Fig. 1 for a diagram of the geometry implied by this profile, Fig. A2 for the corresponding heat map, and Appendix C for a discussion of model parameter uncertainties).

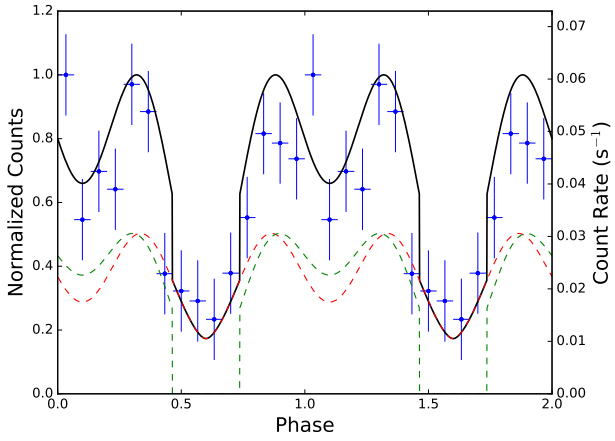

Figure 4. 6-parameter *Polestar* fit for *Chandra* ObsID 1785. In this fit, $i = 62°$ and $\theta = 70°$, producing a double-peaked prfoile.

width increases. For example, Fig. 3 is a fit where $\max(i, \theta) = 54°$, and the resulting width of the peak is roughly three quarters of a phase. Two peaks emerge in the profile when the sum $i + \theta \geq 130°$. An example of this can be found in Fig. 4, where $i + \theta = 132°$.

Examining the histograms for i and θ in the 6-parameter fit (Fig. 5), peaks at $\sim 25°$ are evident along with secondary peaks around 70°. This bimodality is associated with an event that occured in 2002, and will be disucssed in further detail in § 5.

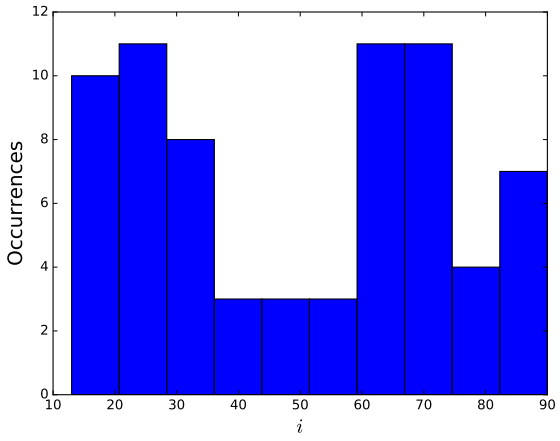

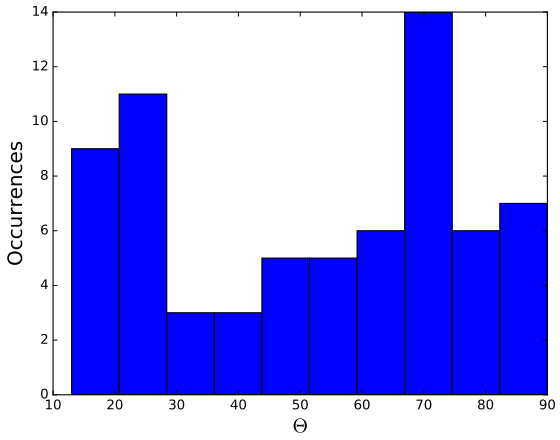

Figure 5. Histograms of i and θ values for the 6-parameter *Polestar* fits.

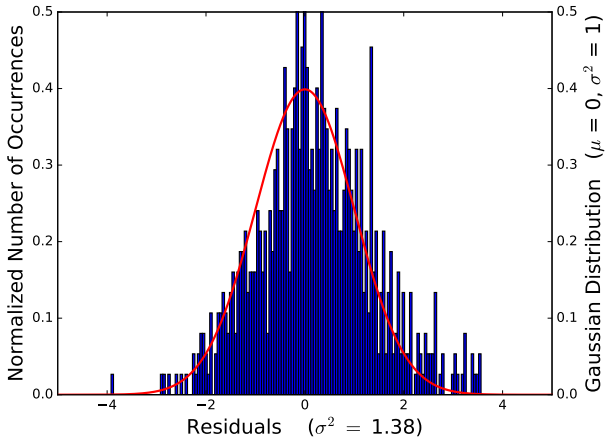

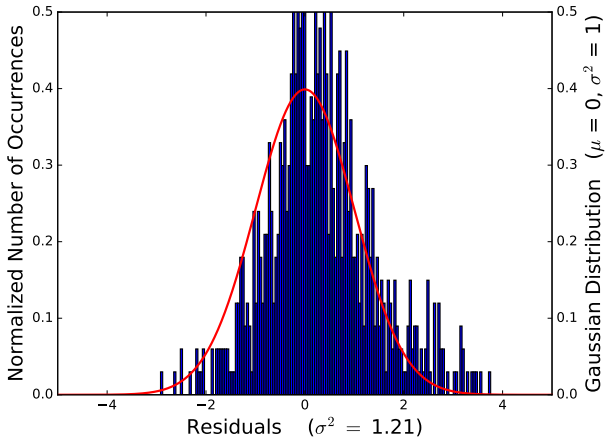

Figure 6. The sum of residuals of all profiles for the 4 (top) and 6 (bottom) parameter *Polestar* fits. The red line is a Gaussian with a mean of zero and a variance of one.

4.3 Statistical Distribution of Profile Fits

An alternate method to χ^2 statistics of quantifying the quality of a fit is to compare the normalized distribution of the sum of its residuals to a standard Gaussian distribution with a mean of zero and a variance of unity (which would represent a perfect fit). This comparison serves as an independent check that the fits are optimal (Andrae et al. 2010). In Fig. 6, the distribution of residuals is compared to the Gaussian distribution for the 4 and the 6 parameter *Polestar* fits. Both sets of residuals adhere to a Gaussian distribution and the variance of the 6 parameter fit is smaller than that of the 4 parameter fit, indicating the expected improvement in fit.

5 TIME EVOLUTION OF PROFILE FITS

To further explore the bimodality present in Figs. 2 & 5 we searched for correlations within the data. Initially we wanted to rule out instrumental bias, and indeed the bimodality was present in each instrument (See Fig. 7). While searching for other explanations we noticed a correlation with time, specifically there appeared to be a change in the fits following the second half of 2002.

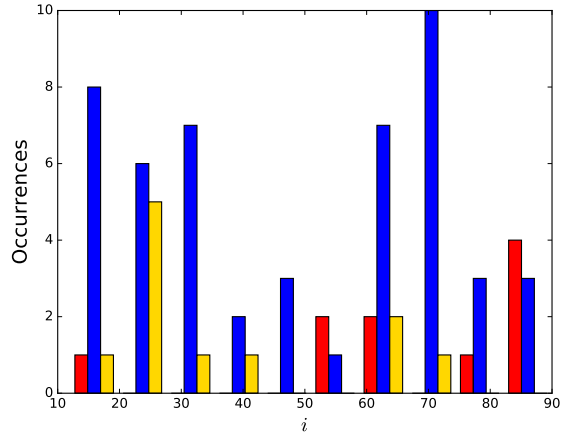

Figure 7. Histogram for inclination i between the different observing instruments. *XMM-Newton* is in red, *Chandra* ACIS-I is in blue, and *Chandra* ACIS-S is in yellow. The distribution is bimodal in each color, implying no instrumental bias.

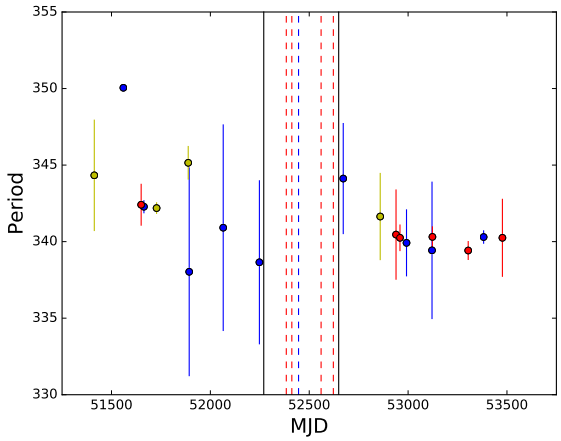

Figure 8. A plot of the change in period for SXP348 over time. As in Fig. 7, blue indicates *Chandra* ACIS-I, yellow indicates *Chandra* ACIS-S, and red indicates *XMM-Newton* EPIC-pn. The span in 2002 where the fit parameters changed is bookended by solid black lines. The red and blue dashed lines indicate observations where the source was detected but lacked significant pulsations. The error bars on the period were calculated following a Monte Carlo approach (see Appendix B). For clarity, observations made on the same or consecutive days have been combined.

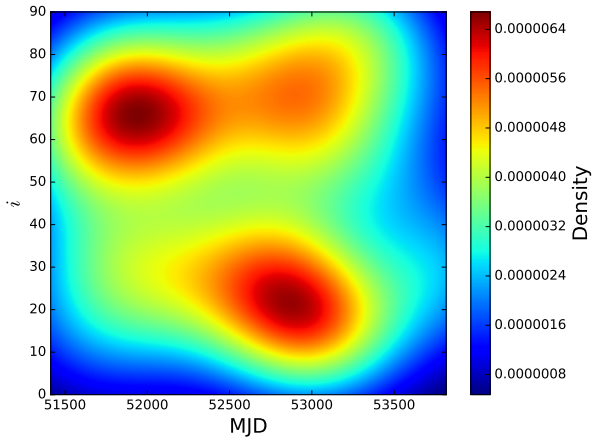

Figure 9. A population density map for the 6-parameter fit in i vs MJD space. Areas with a higher concentration of data points appear redder. The preferred value for i in the fits changes from $\sim 65^\circ$ to $\sim 20^\circ$ during the second half of 2002.

From August 1999 (MJD 51413) to December of 2001 (MJD 52384) SXP348 was observed gradually spinning up. Then in all observations of 2002, with both *Chandra* and *XMM-Newton*, pulsations became undetectable despite the source remaining bright (Fig. 8). When periodic pulsations resumed in February of 2003 (MJD 52671), its period had lengthened, after which it proceeded to consistently spin up again until March of 2006 (MJD 53816). The best-fit parameters for the model changed after this event in 2002 (Fig. 9). Figure 10 gives an example of model fits to profiles directly before and after this event. This puzzling event, cessation of pulsation followed by change of geometry, will be discussed below.

5.1 A Decade of Quiescence

The last time pulsations were detected for SXP348 was in March of 2006 (MJD 53816) with *Chandra* ACIS-I. This source happens to be in the FOV of a *Chandra* calibration target, so there are many pointings containing this system, all the way up to April of 2018. After 2006 the luminosity dropped and the pulsations disappeared, with the final detection of SXP348 as a point-source occuring in February of 2011 (MJD 55603) with *Chandra* ACIS-S (ObsID 12147)(Fig. 11). This observation was much deeper than the surrounding ones, with an exposure time of 149 ksec, yet still no significant pulsations were detected. Other X-ray telescopes, including *RXTE*, *Suzaku*, *Swift*, and *NuSTAR* have also failed to detect any pulsations from this source since 2006.

6 DISCUSSION

We designed our geometric model *Polestar* (Paper I) as a predictive tool with the intention of probing the orientations of various X-ray pulsars and the geometries of their emission regions, as well as detecting parameter changes during the state transitions of the sources. In this work, we analyzed in detail the *Polestar* fits for SXP348, a Be/X-ray pulsar for which similar studies have not been attempted previously, providing little in the literature to guide our search for the best-fit geometric configuration. In contrast, X-ray spectra from this source have been studied in detail and the pulse period has been measured multiple times (Yokogawa & Koyama 1998; Haberl & Pietsch 2004; McGowan et al. 2007). Our statistical analysis of the pulse profiles extracted from our pipeline indicates that an event in 2002 lead to a change in the best-fit model parameters. During this event SXP348 was not producing observable periodic emission, and it is likely that the emission regions themselves were undergoing a transformation. This transformation led to the hot spots having a different geometry, eventually leading to X-ray quiescence by 2012.

In the past two years, SXP348 has not been observed as its home wing of the SMC has not been targeted by *Chandra* or *XMM-Newton*. New observations are needed to determine whether the source is still below the propeller line or accretion has recently resumed. It is possible that the magnetosphere has expanded and the strong magnetic field has shut down accretion altogether.

The emergence of fan-beam behavior is marked by the introduction of steep features into the modeled pulse profiles. While previous models have considered the effect of fan-beam emission on the profile (e.g., Karino 2007, among others), they primarily focused on the emergence of secondary peaks rather than on the abrupt steepening of primary peaks. We argue that the latter effect also has predictive power and it gives us a new tool for determining source-specific critical luminosities and the onset of fan-beam emission. Due to an $L_{X,max}$ on the order of 10^{36} erg s^{-1}, it is

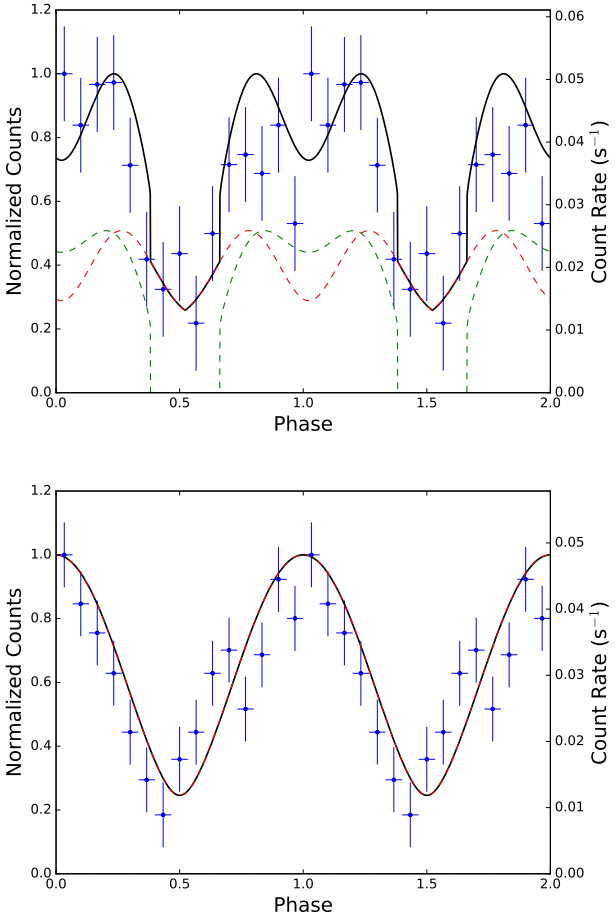

Figure 10. A comparison of two profiles fits, one before the summer of 2002 (top: *Chandra* ObsID 2843), and one after (bottom: *Chandra* ObsID 3520). Notice that the double-peaked structure (associated with $i + \theta \geq 130°$) has vanished.

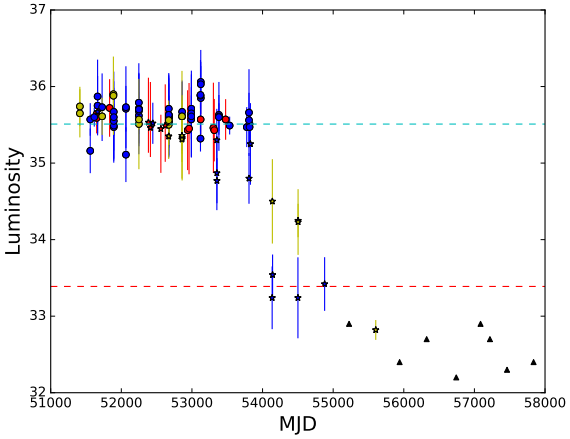

Figure 11. All of the detections for SXP348. As in previous figures, red indicates *XMM-Newton* EPIC-PN, blue is *Chandra* ACIS-I, and yellow is *Chandra* ACIS-S. The circles indicate detection of pulsations and the stars indicate detections of the source without detected pulsations. The black triangles are upper limits for non-detections. The dashed lines represent the propeller line for various magnetic field strengths following the formula found in Christodoulou et al. (2016) for a NS with a mass of 1.4 $M_\odot$, a radius of 10 km, and a period of 342 s. The red line is for B = 10 TG and the cyan line is from Table 3 in Klus et al. (2014) as their calculated lower limit for this source at B = 115 TG. Luminosities are displayed in erg s^{-1}, $\log_{10}$ scale.

unlikely that SXP348 produces significant fan-beam radiation and thus we were only left to infer a lower bound for the critical luminosity at $\sim 5 \times 10^{36}$ erg s^{-1}.

While the best-fit parameters changed during the event in 2002, it is reasonable to assume that the inclination angle (i) didn't physically change. The only physical mechanism for a change in i would be a precession of the spin axis, which would produce a periodic change in i of a small magnitude, which is not indicated by the fitting. However, the change in parameters does suggest there was some physical change in the system that resulted in the disappearance of pulsed emission accompanied by only a small drop in luminosity. One possibility is that the beam opening angle changed, causing it to not pass through the line of sight for multiple rotations, coupled with increased non-pulsed emission from excess spherical accretion, or reprocessing/scattering. Another possibility could be a change in the composition or orientation of the decretion disk, obscuring the pulsed emission. This episode occurred in conjunction with a spin-down, and once pulsations resumed the emission geometry had changed. One possible mechanism for this change in geometry could be moving hot spots within an elongated accretion column, as suggested in Miller (1996).

Since i should remain static, we suggest that there is a most-likely geometry for this system, with i at a value of $\sim 65° \pm 3.5°$and $\theta \simeq 20° \pm 7.0°$. For a detailed discussion on the uncertainties reported with these values, see Appendix C. This most-likely geometry is similar to the diagram in Fig. 1.

In the interest of completeness we mention that other modelling efforts suggest that the height of the accretion column may reach a point ($\sim$ 3-5 km above the NS surface) that a magnetic pole's maximum contribution could occur at the point that it is furthest from the observer, assuming fan-beam emission (Pottschmidt et al. 2018). This is due to space-time being warped enough in the presence of such a strong gravity well that photons eventually escape on the opposite side of the NS, akin to the "Einstein Ring" phenomenon observed around distant galaxies and BHs. Again, it is unlikely that the accretion column would reach such a height during the luminosity states that this particular source has been observed in (Becker et al. 2012). For this reason the height of the accretion column was not included as a parameter in the fits performed for this paper.

7 CONCLUSIONS

We extracted and analyzed 71 individual pulse profiles for the SMC X-ray Pulsar SXP348 from *Chandra* and *XMM-Newton* archival data spanning two decades of observations. Each of these profiles were fitted with a four and six free parameter version of *Polestar*. This pulsar experienced an

event in 2002 which manifested itself as a dramatic change in the best-fit parameters of the model, accompanied by a possible spin-down. Although in the field of view for observations through 2018, this source has not been detected since 2011, and no significant pulsations have been measured since 2006, indicating it dropped below the propeller line. We suggest a most-likely geometry for this source of i $\simeq 65^\circ \pm 3.5^\circ$and $\theta \simeq 20^\circ \pm 7.0^\circ$.

ACKNOWLEDGEMENTS

This work was facilitated by NASA ADAP grants NNX14-AF77G and 80NSSC18K0430, with UMASS Lowell in conjunction with LoCSST (Lowell Center for Space Science and Technology). The authors would also like to thank W. Ho, S. Falkner and H. Klus for their helpful discussions, as well as the annonymous referee whose detailed notes improved this paper greatly.

REFERENCES

Andrae, R., Schulze-Hartung, T., & Melchior, P. 2010, arXiv:1012.3754v1
Attia, A., 2011, Ap&SS, 334, 103
Basko, M. M., & Sunyaev, R. A. 1976, MNRAS, 175, 395
Becker, P. A., Klochkov, D., Schonherr, G., et al. 2012, A&A, 544, A123
Beloborodov, A. M. 2002, ApJ, 566, L85
Bianchi, P., Hachem, W., & Iutzeler, F. 2014, arXiv:1407.0898
Cappallo, R., Laycock, S. G. T., & Christodoulou, D. M. 2017, PASP, 129, 124201 (Paper I)
Carbary, J. F., Mitchell, D. G., Krimigis, S. M., & Krupp, N. 2011, GRL, 38, 24
Christodoulou, D. M., Laycock, S. G. T., Yang, J., & Fingerman, S. 2016, ApJ, 829, 30
Coe, M. J., Edge, W. R. T., Galache, J. L., & McBride, V. A. 2005, MNRAS, 356, 502
Coe, M. J., & Orosz, J. A. 2000, MNRAS, 311, 169
Eger, P., & Haberl, F. 2008, A&A, 491, 841
Evans, C. J., Howarth, I. D., Irwin, M. J., Burnley, A. W., & Harries, T. J. 2004, MNRAS, 353, 601
Falkner, S. 2018, PhD Thesis, University of Erlangen-Nürnberg
Ferrigno, C., Falanga, M., Bozzo, E., et al. 2011, A&A, 532, A76
Haberl, F., & Pietsch, W. 2004, A&A, 414, 667
Haschke, R., Grebel, E. K., & Duffau, S. 2012, AJ, 144, 107
Horne, J. H., Baliunas, S. L. 1986, ApJ, 302, 757
Hughes, J. P., & Smith, R. R. 1994, AJ, 107, 4
Israel, G. L., Stella, L., Campana, S., et al. 1998, IAUC, 6999, 1
Israel, G. L., et al. 2000, ApJ, 531, 131
Hilditch, R. W., Howarth, I. D., & Harries, T. J. 2005, MNRAS, 357, 304
Karino, S., 2007, PASJ, 59, 961
Klus, H., Ho, W. C. G., Coe, M. J., Corbet, R. H. D., & Townsend, L. J. 2014, MNRAS, 437, 4
Kovacs, G. 1981, Ap&SS, 78, 175
Lomb, N. R. 1976, Ap&SS, 39, 447
McGowan, K. E., Coe, M. J., Schurch, M., et al. 2007, MNRAS, 376, 759
Miller, G. S. 1996, ApJ, 468, L29
Mushtukov, A. A., Verhagen, P. A., Tsygankov, S. S., et al. 2018, MNRAS, 474, 5425
Pottschmidt, K., Hemphill, P. B., Wolff, M. T., et al. 2018, AAS meeting, 231, 243.11

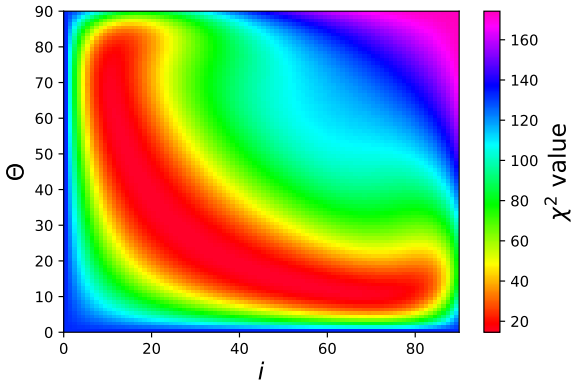

Figure A1. Four parameter *Polestar* fit of *XMM-Newton* ObsID 0135721701.

Rajoelimanana, A. F., Charles, P. A., & Udalski A. 2011, MNRAS, 413, 1600
Reig, P., Milonaki, F. 2016, A& A, 594, A45
Reig, P. 2011, Ap&SS, 332, 1
Reig, P., Nespoli, E. 2013, A& A, 551, A1
Rothschild, R. E., Kuhnel, M., Pottschmidt, K., et al. 2017, MNRAS, 466, 2752
Scargle, J. D. 1982, ApJ, 263, 835
Schmidtke, P. C., & Cowley, A. P. 2006, AJ, 13, 919
Schurch, M. P. E., Coe, M. J., McGowan, K. E., et al. 2007, MNRAS, 381, 1561
Tseng, P. 2001, JOTA, 109, 475
VanderPlas, J. T., 2017, ApJS, 236, 1
Vybornov, V., Klochkov, D., Gornostaev, M. 2017, A& A, 601, A126
Yang, J., Laycock, S. G. T., Christodoulou, D. M., et al. 2017, ApJ, 839, 119
Yokogawa, J., & Koyama, K. 1998, IAUC, 7009, 3
Zavlin, V. E., Pavlov, G. G., Shibanov, Y. A., & Ventura, J. 1995, A&A, 297, 441

APPENDIX A: VISUALIZATION OF FIT PARAMETER SPACE

Heat maps were produced for both the 4 and 6 parameter fits. Slices of the parameter spaces were examined by allowing two parameters to vary while keeping the rest of the parameters fixed at their best-fit values. The color corresponds to the χ^2 value, with lower values (i.e. better fits) appearing redder. The following is a comparison of the features for two heat maps of the same profile in i and θ space.

In Fig. A1, the four parameter fit of *XMM-Newton* ObsID 0135721701 displays the degeneracy between i and θ as a diagonal line of symmetry through the figure. Notice the gradients and transitions are all smooth due to only a cosine beaming function being used.

In Fig. A2, the diagonal symmetry remains (as it should for any antipodal hot-spot arrangement), but there are sharp transitions as well as more shallow lines of demarcation in the gradients. Both of these features are due to the fan-beam component, but they have different causal origins. The very sharp features evident in the diagonal line travelling from the ($\theta = 0$, $i = 45$) point to the ($\theta = 45$, $i = 0$) point represent

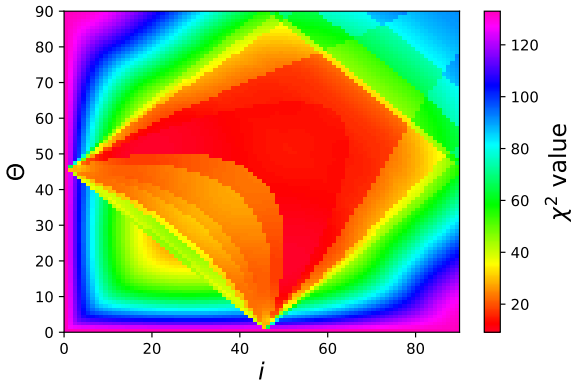

Figure A2. Six parameter *Polestar* fit of *XMM-Newton* ObsID 0135721701. For best fit see Fig. 3.

a pole crossing the terminator. Here a pole that previously had no contribution to the overall profile is suddenly making a large contribution. The more subtle lines (i.e. the parabolic ones anchored to the above two points) are artefacts of the binning procedure used to create the profiles. Once vertical lines become possible in the model profiles (e.g., Fig. 3), there will also be sharp lines in the corresponding heat maps as the profile crosses over bin edges.

APPENDIX B: DETERMINING PERIOD UNCERTAINTIES

When using a Lomb-Scargle Periodogram (Lomb 1976; Scargle 1982) to determine the period of a pulsar the uncertainty in the measured period is typically estimated using the formula of Kovacs (1981), as popularized by Horne & Baliunas (1986). This prescription is somewhat lacking, as uncertainties tend to be associated with aliasing and false peaks present in the background, and are not necessarily present near the given period. For a thorough discussion of this, see VanderPlas (2017).

We used a Monte Carlo approach similar to Carbary et al. (2011). The maximum-peak ratio (MPR) was calculated for all periodograms, defined as the ratio of the height of the maximum peak to the mean of the heights of all other peaks. These MPR values formed a distribution with a mean of 17.98 and a standard deviation of 12.56 (Fig. B1).

1000 artificial light curves were then created for SXP348 with a period of 350 sec with enough Gaussian noise added to them to produce an MPR distribution with the same mean and variance as the MPR distribution of the data. The identified periods of these artificial light curves were then plotted as a function of their MPR (Fig. B2), providing a reference for periodicity error given the calculated MPR of the data. The envelope at 1σ is described by equation B1, utilized to calculate all period uncertainties reported in this paper.

$$\text{Period Uncertainty} = \pm\ 10e^{-\frac{3}{20}\times MPR}\ \text{sec} \qquad \text{(B1)}$$

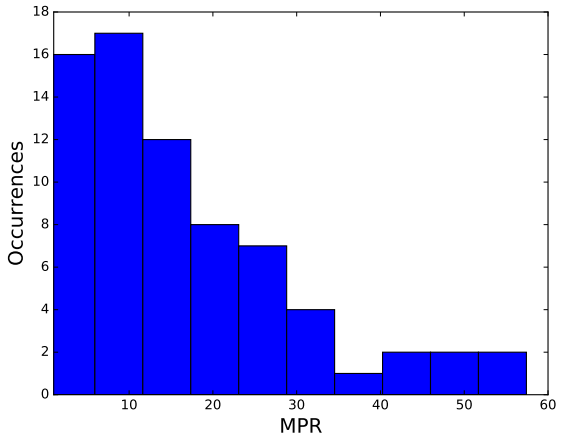

Figure B1. A histogram of the maximum-peak ratios calculated for each periodogram.

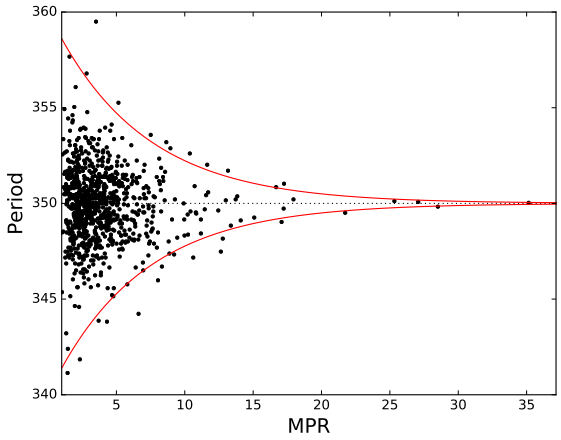

Figure B2. A plot of spread in period as a function of MPR for 1000 artificial light curves. The green and blue lines are one and two percent of the given period of 350 sec, respectively. The red line is the envelope at 1σ, and was used to calculate the period uncertainties in this paper.

APPENDIX C: *Polestar* PARAMETER UNCERTAINTIES

Parameter confidence intervals were estimated using bootstrap resampling. To suggest a range of uncertainty for the parameters we have incorporated a Monte Carlo examination of two profiles used in this study, one with high signal-to-noise (*Chandra* ObsID 1543) and one with low signal-to-noise (*Chandra* ObsID 444).

Each pulse profile is binned at fifteen data points per phase. For each of these fifteen points a random value was selected from a normal distribution with a mean of the count value of the given point and a standard deviation equal to the error on that value. In this fashion one hundred different profiles were created from each observation's folded pulse profile. Then each profile was fit with *Polestar*, giving distributions for each parameter value in the fit (Table C1).

Table C1. Table of parameter uncertainties for a low and high signal pulse profile.

ObsID		i	θ	ϕ	P_{cos}	P_{sin}	P_{rat}
444	Mean:	53.9	16.6	306.0	1.0	3.0	0.1
low	σ:	3.5	8.8	8.0	0.7	0.1	0.2
1543	Mean:	66.8	66.5	311.2	1.6	2.5	0.2
high	σ:	3.4	6.1	2.7	1.1	1.1	0.1

The reported uncertainty is 1σ of the resulting parameter distribution.

APPENDIX D: FITTING TABLES

This paper has been typeset from a TEX/LATEX file prepared by the author.

Table D1. *Polestar* parameters with 4 free variables.

ObsID	Instr.	MJD	i	θ	ϕ	P_{cos}	L_X	χ^2	Error
5141	CH-I	53125	27.0	30.0	152.0	3.0	11.42	12.27	0.16
5142	CH-I	53125	18.0	40.0	164.0	3.0	10.62	4.05	0.17
1308	CH-S	51888	24.0	60.0	224.0	3.0	8.02	5.70	0.13
5144	CH-I	53121	30.0	30.0	22.0	3.0	7.74	11.13	0.16
5143	CH-I	53121	28.0	30.0	196.0	3.0	7.64	12.64	0.16
1311	CH-S	51888	70.0	26.0	16.0	3.0	7.62	13.03	0.12
444	CH-I	51664	26.0	33.0	124.0	3.0	7.48	12.53	0.16
5140	CH-I	53125	18.0	41.0	22.0	3.0	7.11	9.43	0.17
2837	CH-I	52248	23.0	78.0	64.0	3.5	6.21	22.39	0.12
445	CH-I	51664	45.0	85.0	88.0	2.0	5.60	11.99	0.13
1231	CH-S	51413	22.0	41.0	316.0	3.5	5.47	18.27	0.14
1543	CH-I	52065	25.0	33.0	160.0	3.0	5.36	20.16	0.16
1785	CH-I	51728	33.0	26.0	98.0	3.0	5.33	28.36	0.15
0106860101	EPIC-pn	51834	60.0	69.0	80.0	3.0	5.21	18.88	0.16
1542	CH-I	52065	30.0	31.0	262.0	2.5	5.17	11.47	0.16
2839	CH-I	52248	61.0	78.0	340.0	2.0	5.14	38.60	0.13
5149	CH-I	52992	85.0	32.0	120.0	3.0	5.14	34.68	0.12
3538	CH-I	52672	60.0	13.0	94.0	3.5	5.14	22.89	0.14
2836	CH-I	52248	87.0	23.0	344.0	3.5	5.11	13.22	0.14
2842	CH-I	52249	37.0	66.0	20.0	2.0	5.03	11.75	0.14
2838	CH-I	52248	29.0	30.0	210.0	3.0	4.81	18.67	0.15
1313	CH-I	51893	66.0	66.0	52.0	2.0	4.68	30.62	0.13
3534	CH-I	52861	14.0	50.0	50.0	3.5	4.65	14.87	0.16
6754	CH-I	53808	70.0	70.0	22.0	2.0	4.58	18.56	0.14
138	CH-S	51413	60.0	14.0	20.0	3.5	4.50	9.33	0.15
5150	CH-I	52992	40.0	18.0	158.0	3.0	4.42	10.10	0.17
0123110201	EPIC-pn	51650	60.0	88.0	266.0	2.0	4.37	13.18	0.08
5148	CH-I	52992	34.0	23.0	40.0	3.5	4.36	12.51	0.15
3540	CH-I	52672	22.0	50.0	308.0	3.5	4.31	33.78	0.13
3542	CH-I	52672	85.0	33.0	78.0	3.0	4.28	9.39	0.14
6051	CH-I	53382	60.0	13.0	120.0	3.5	4.24	15.47	0.15
5147	CH-I	52992	83.0	46.0	216.0	2.0	4.21	14.03	0.15
2835	CH-I	52248	84.0	53.0	244.0	2.0	4.20	13.88	0.16
3532	CH-I	52861	60.0	13.0	334.0	3.5	4.12	15.89	0.15
6053	CH-I	53382	86.0	31.0	192.0	3.5	4.12	14.86	0.14
1789	CH-S	51728	31.0	31.0	358.0	2.5	4.11	19.88	0.16
3547	CH-S	52859	29.0	33.0	192.0	2.5	4.11	8.72	0.17
5151	CH-I	52992	17.0	41.0	76.0	3.0	4.05	9.88	0.18
3535	CH-I	52671	83.0	60.0	160.0	2.0	4.04	12.30	0.14
420	CH-I	51617	25.0	32.0	210.0	3.0	4.02	13.30	0.16
1317	CH-I	51893	78.0	60.0	172.0	3.0	4.00	25.30	0.14
6054	CH-I	53382	63.0	78.0	176.0	2.0	3.99	20.07	0.15
3537	CH-I	52672	75.0	74.0	122.0	2.0	3.92	19.65	0.15
0123110301	EPIC-pn	51651	30.0	89.0	112.0	2.5	3.87	17.85	0.11
3536	CH-I	52672	31.0	30.0	120.0	2.5	3.85	8.42	0.17
48	CH-I	51560	30.0	75.0	94.0	3.5	3.75	49.89	0.10
5146	CH-I	52989	68.0	60.0	160.0	2.0	3.74	25.19	0.14
2844	CH-S	52249	41.0	24.0	92.0	3.5	3.72	28.08	0.13
0135721901	EPIC-pn	53123	90.0	70.0	46.0	2.0	3.71	40.59	0.07
0159360601	EPIC-pn	53477	50.0	87.0	312.0	2.0	3.69	19.84	0.08
6752	CH-I	53808	33.0	30.0	336.0	2.5	3.62	6.74	0.17
3524	CH-S	52671	17.0	40.0	282.0	3.0	3.60	8.83	0.17
1316	CH-I	51893	73.0	74.0	56.0	2.0	3.52	9.89	0.17
3520	CH-S	52671	32.0	32.0	40.0	3.5	3.50	14.29	0.14
3539	CH-I	52672	30.0	67.0	124.0	3.0	3.47	40.82	0.11
2843	CH-S	52249	18.0	40.0	138.0	3.0	3.24	11.24	0.17
6748	CH-I	53816	30.0	87.0	308.0	3.5	3.23	18.04	0.15
3519	CH-S	52671	32.0	25.0	346.0	3.5	3.18	9.91	0.15
6060	CH-I	53534	20.0	40.0	246.0	2.5	3.12	10.05	0.17
1315	CH-I	51893	20.0	74.0	46.0	3.5	3.09	32.32	0.12
6749	CH-I	53816	15.0	42.0	64.0	3.5	2.97	11.14	0.17
5486	CH-I	53776	40.0	19.0	40.0	3.0	2.95	14.62	0.17
1314	CH-I	51893	30.0	87.0	126.0	3.5	2.92	10.71	0.18
0135722001	EPIC-pn	53304	86.0	46.0	96.0	2.0	2.86	38.72	0.07
0152280501	EPIC-pn	52959	85.0	65.0	270.0	2.0	2.85	36.31	0.08
0135721701	EPIC-pn	52959	18.0	40.0	280.0	3.0	2.77	14.56	0.13
0135721501	EPIC-pn	52939	52.0	86.0	14.0	2.0	2.69	19.81	0.09
0135722201	EPIC-pn	53316	59.0	84.0	150.0	2.0	2.68	13.80	0.14
5145	CH-I	53121	62.0	80.0	328.0	3.5	2.09	33.01	0.16
49	CH-I	51560	50.0	86.0	56.0	3.0	1.46	8.44	0.21
1534	CH-I	52065	69.0	69.0	162.0	3.5	1.29	18.37	0.19

Pulse profiles fit with 4-parameter *Polestar*, ranked according to luminosity. The columns are Observation ID, the observing instrument (CH-I and CH-S are *Chandra* ACIS-I and ACIS-S respectively, and EPIC-pn is the *XMM-Newton* EPIC-pn detector), Modified Julian Date (MJD), the inclination angle (i), the angle between the primary hot spot and the spin axis (θ), the angle between the primary hot spot and an (arbitrary) phase = 0 point (ϕ), the power of the cosine beaming function (P_{cos}), the X-ray luminosity in units of 10^{35}erg s^{-1}(L_X), the chi-squared statistic value (χ^2), and the mean count error in units of counts s^{-1}. All angles are given in units of degrees.

Table D2. *Polestar* parameters with 6 free variables.

ObsID	Instr.	MJD	i	θ	ϕ	P_{cos}	P_{sin}	P_{rat}	L_X	χ^2	Error
5141	CH-I	53125	12.0	20.0	332.0	1.0	3.0	0.0	11.42	11.33	0.16
5142	CH-I	53125	26.0	18.0	340.0	1.0	3.0	0.1	10.62	4.40	0.17
1308	CH-S	51888	24.0	60.0	224.0	3.0	1.0	1.0	8.02	5.70	0.13
5144	CH-I	53121	16.0	16.0	204.0	1.0	3.0	0.0	7.74	7.73	0.16
5143	CH-I	53121	14.0	14.0	16.0	1.0	3.0	0.0	7.64	9.31	0.16
1311	CH-S	51888	70.0	26.0	16.0	3.0	1.0	1.0	7.62	13.03	0.12
444	CH-I	51664	54.0	20.0	300.0	1.0	3.0	0.1	7.48	9.19	0.16
5140	CH-I	53125	64.0	54.0	188.0	1.0	3.0	0.3	7.11	6.59	0.17
2837	CH-I	52248	30.0	74.0	64.0	3.0	1.0	1.0	6.21	22.82	0.12
445	CH-I	51664	84.0	54.0	92.0	3.0	1.0	0.9	5.60	9.22	0.13
1231	CH-S	51413	20.0	20.0	136.0	1.0	3.0	0.0	5.47	17.68	0.14
1543	CH-I	52065	62.0	70.0	312.0	1.0	3.0	0.3	5.36	13.41	0.16
1785	CH-I	51728	62.0	70.0	144.0	1.5	3.0	0.2	5.33	20.04	0.15
0106860101	EPIC-pn	51834	12.0	36.0	256.0	1.0	2.0	0.0	5.21	26.86	0.16
1542	CH-I	52065	30.0	40.0	264.0	3.0	1.0	0.9	5.17	9.78	0.16
2839	CH-I	52248	60.0	78.0	344.0	3.0	1.0	0.9	5.14	34.33	0.13
5149	CH-I	52992	66.0	72.0	120.0	3.0	3.0	0.9	5.14	31.78	0.12
3538	CH-I	52672	34.0	50.0	88.0	3.0	1.0	0.9	5.14	20.99	0.14
2836	CH-I	52248	62.0	78.0	344.0	3.0	1.0	0.9	5.11	10.11	0.14
2842	CH-I	52249	42.0	60.0	20.0	3.0	3.0	0.9	5.03	11.03	0.14
2838	CH-I	52248	14.0	20.0	36.0	1.0	3.0	0.0	4.81	17.07	0.15
1313	CH-I	51893	68.0	68.0	52.0	3.0	1.0	0.9	4.68	29.84	0.13
3534	CH-I	52861	14.0	14.0	224.0	1.0	3.0	0.0	4.65	14.44	0.16
6754	CH-I	53808	70.0	70.0	24.0	2.0	1.0	1.0	4.58	18.62	0.14
138	CH-S	51413	62.0	16.0	20.0	3.0	1.0	1.0	4.50	9.40	0.15
5150	CH-I	52992	20.0	18.0	332.0	1.0	3.0	0.1	4.42	8.87	0.17
0123110201	EPIC-pn	51650	64.0	86.0	264.0	3.0	1.0	0.9	4.37	9.18	0.08
5148	CH-I	52992	32.0	48.0	40.0	3.0	1.0	0.9	4.36	11.50	0.15
3540	CH-I	52672	24.0	26.0	136.0	1.0	2.0	0.2	4.31	30.49	0.13
3542	CH-I	52672	68.0	70.0	72.0	3.0	3.0	0.9	4.28	9.05	0.14
6051	CH-I	53382	16.0	18.0	296.0	1.0	3.0	0.0	4.24	15.13	0.15
5147	CH-I	52992	78.0	58.0	220.0	3.0	1.0	0.9	4.21	12.63	0.15
2835	CH-I	52248	90.0	90.0	340.0	1.0	3.0	0.6	4.20	16.06	0.16
3532	CH-I	52861	50.0	34.0	336.0	3.0	1.0	0.9	4.12	14.46	0.15
6053	CH-I	53382	84.0	40.0	192.0	3.0	1.0	1.0	4.12	15.12	0.14
1789	CH-S	51728	34.0	34.0	184.0	1.0	2.0	0.4	4.11	18.17	0.16
3547	CH-S	52859	16.0	52.0	12.0	1.0	3.0	0.0	4.11	7.24	0.17
5151	CH-I	52992	20.0	60.0	256.0	1.0	3.0	0.0	4.05	5.68	0.18
3535	CH-I	52671	80.0	90.0	340.0	3.0	1.0	0.9	4.04	13.02	0.14
420	CH-I	51617	12.0	12.0	32.0	1.0	3.0	0.0	4.02	10.56	0.16
1317	CH-I	51893	78.0	60.0	172.0	3.0	1.0	1.0	4.00	25.30	0.14
6054	CH-I	53382	70.0	76.0	176.0	3.0	3.0	0.9	3.99	19.04	0.15
3537	CH-I	52672	74.0	70.0	304.0	3.0	3.0	0.9	3.92	20.19	0.15
0123110301	EPIC-pn	51651	60.0	82.0	20.0	2.0	3.0	0.5	3.87	15.92	0.11
3536	CH-I	52672	12.0	22.0	300.0	1.0	3.0	0.0	3.85	7.94	0.17
48	CH-I	51560	34.0	72.0	96.0	3.0	1.0	1.0	3.75	50.56	0.10
5146	CH-I	52989	64.0	50.0	148.0	3.0	3.0	0.9	3.74	23.48	0.14
2844	CH-S	52249	24.0	22.0	280.0	1.0	3.0	0.3	3.72	13.94	0.13
0135721901	EPIC-pn	53123	88.0	52.0	136.0	1.0	3.0	0.4	3.71	32.27	0.07
0159360601	EPIC-pn	53477	86.0	62.0	220.0	1.0	3.0	0.5	3.69	21.25	0.08
6752	CH-I	53808	32.0	26.0	336.0	3.0	1.0	1.0	3.62	6.76	0.17
3524	CH-S	52671	26.0	16.0	104.0	1.0	3.0	0.1	3.60	8.62	0.17
1316	CH-I	51893	66.0	78.0	64.0	3.0	1.0	0.9	3.52	9.36	0.17
3520	CH-S	52671	24.0	16.0	180.0	0.5	3.0	0.0	3.50	13.59	0.14
3539	CH-I	52672	68.0	30.0	124.0	3.0	1.0	1.0	3.47	40.85	0.11
2843	CH-S	52249	64.0	64.0	172.0	0.5	3.0	0.4	3.24	6.69	0.17
6748	CH-I	53816	38.0	86.0	308.0	3.0	1.0	1.0	3.23	18.21	0.15
3519	CH-S	52671	36.0	26.0	344.0	3.0	1.0	1.0	3.18	9.94	0.15
6060	CH-I	53534	50.0	20.0	68.0	1.0	3.0	0.4	3.12	7.49	0.17
1315	CH-I	51893	32.0	50.0	52.0	3.0	1.0	1.0	3.09	33.98	0.12
6749	CH-I	53816	26.0	50.0	64.0	3.0	1.0	0.9	2.97	9.48	0.17
5486	CH-I	53776	20.0	20.0	212.0	1.0	2.0	0.0	2.95	10.88	0.17
1314	CH-I	51893	70.0	76.0	128.0	3.0	3.0	0.9	2.92	11.15	0.18
0135722001	EPIC-pn	53304	52.0	86.0	96.0	3.0	1.0	0.9	2.86	29.06	0.07
0152280501	EPIC-pn	52959	88.0	70.0	92.0	3.0	1.0	0.9	2.85	38.10	0.08
0135721701	EPIC-pn	52959	50.0	20.0	280.0	1.5	3.0	0.3	2.77	9.18	0.13
0135721501	EPIC-pn	52939	52.0	86.0	12.0	2.0	1.0	1.0	2.69	20.06	0.09
0135722201	EPIC-pn	53316	88.0	70.0	332.0	3.0	1.0	0.9	2.68	13.99	0.14
5145	CH-I	53121	74.0	74.0	144.0	3.0	1.0	1.0	2.09	35.97	0.16
49	CH-I	51560	50.0	86.0	56.0	3.0	1.0	1.0	1.46	8.44	0.21
1534	CH-I	52065	68.0	68.0	164.0	3.0	1.0	1.0	1.29	20.55	0.19

Profiles fit with 6-parameter *Polestar*. All of the columns are the same as in table D1 with the addition of the power of the sine beaming function (P_{sin}), and the ratio between the cosine and sine beaming functions (P_{rat}).